RIGOROUS NONLINEAR ELECTROSTATIC SIMULATION OF ATOM PROBE TOMOGRAPHY

A Dissertation
Presented to
The Academic Faculty

By

Qihua Zhang

In Partial Fulfillment
of the Requirements for the Degree
Master of Science in the
School of Electrical and Computer Engineering

Georgia Institute of Technology

August 2020

RIGOROUS NONLINEAR ELECTROSTATIC SIMULATION OF ATOM PROBE TOMOGRAPHY

Approved by:

Dr. Benjamin Klein, Advisor
School of Electrical and Computer Engineering
Georgia Institute of Technology

Dr. Stephen Ralph
School of Electrical and Computer Engineering
Georgia Institute of Technology

Dr. Azadeh Ansari
School of Electrical and Computer Engineering
Georgia Institute of Technology

Date Approved: July 21, 2020

Everything negative – pressure, challenges – is all an opportunity for me to rise.

Kobe Bryant

ACKNOWLEDGEMENTS

I would like to thank my thesis advisor, Dr. Benjamin Klein, who accepted me as a research student in January 2017, has guided me through two research projects, and has provided support for my research career ever since. He has also provided the ultimate support and motivation for me on pursuing my goal. I would also like to thank Dr. Norman Sanford from National Institute of Standards and Technology for the opportunity of my participation in this wonderful project. I am absolutely grateful for the experience I got throughout the last three years in research.

I would also like to acknowledge Dr. Stephen Ralph and Dr. Azadeh Ansari for their commitment to sit on the thesis committee and their support.

Additionally, I would like to thank my parents, my grandparents for their unconditional support and encouragement. It is their assistance that gives me coverage to be what I want to be. Finally, to my girlfriend Sophia, thank you for bringing joy, love, and hope to my life.

TABLE OF CONTENTS

LIST OF TABLES

LIST OF FIGURES

SUMMARY

Atom probe has been used for material research since its first introduction in 1967[1]. While most of the materials researched in atom probe tomography (APT) were metals, recent studies with APT have focused on less-conductive materials such as semiconductors and dielectrics. In this thesis, Gallium nitride (GaN) is used as atom tip placed under APT environment and is studied using mathematical simulations.

A simulation model is created and studied in order to characterize the charge- and field-related behaviors of GaN tip under an APT environment. To calculate such behaviors, a discrete, nonlinear mathematical method for solving self-consistent Poisson's equation in electrostatics is used in this thesis. Additionally,a highly-detailed model of the environment surrounding the atom probe is explained in order to provide rigorous simulations and valid results. A pre-developed program, 'Triangle', is used in this project to provide fine data mesh of the model.

On-axis electric field and mobile charge density within the tip area are the desired results for analysis, where an important scale factor, k-factor, used in classifying how materials behave in APT, is calculated. Comparisons are made with models with varied either the radius of the semiconductor tip or the doping concentration within the tip to form controlled group simulations. By studying simulated results, an inversion layer of positive charges has been observed in an unintentional doped GaN tip starting at 23 volts contact voltage difference, which explains why GaN tip exhibits close similarities as metallic tips by comparing their k-factor. To prove its validity, an imaginary material, 'Insulator-GaN', which bears the same parameters as GaN except it is an insulator, is made for simulation. Such creation provides direct comparison on charge density where inversion layer is observed in the semiconductor-GaN and not in the 'Insulator-GaN'.

CHAPTER 1
INTRODUCTION

Atom probe tomography (APT) is a three-dimensional (3D) material analysis technique that has the capability of imaging position-sensitive structure of materials at the atomic scale as well as classify their chemical composition. A typical APT offers a lateral resolution of 0.3-0.5nm and a depth resolution 0.1-0.3nm in theory [2]. The application of semiconductor material analysis using APT has become popular due to the needs of material advancement and semiconductor device optimization. Experimental teams at the National Institute of Standards and Technology (NIST) have employed such machine into the characterization of III-V semiconductor materials. The main purpose of this project is the use of an nonlinear mathematical implementation of Poisson's electrostatic equations to simulate the field and charge behavior surrounding the apex of the specimen tip. The field evaporation process depends strongly upon these quantities. N-doped Gallium Nitride (GaN) is the main specimen material to be simulated and studied in this project. An environment containing the components of APT: semiconductor tip, bottom metallic layer and top local electrode layer will be designed and modeled in MATLAB and constructed into fine triangular meshes using "Triangle", a Two-Dimensional Quality Mesh Generator [3, 4]. A 3D cylindrically symmetric model is used for simulation instead of a full 3D model in order to make the simulations faster and less resource-intensive. The simulated electrostatic potential has been used to calculate the on-axis electric field strength near the tip apex, and the charge distribution within the semiconductor tip. These are the results which will be presented. Furthermore, comparisons and analysis will be made between the behavior of doped semiconductor and insulating materials. An 'insulator-GaN', which was insulating, was created for study and clarification the conditions under which the metallic approximation is valid. This thesis will also discuss the future work of the project, which

include 2D planar model simulation with the study of spontaneous polarization, a material property of III-Nitride semiconductors.

CHAPTER 2
BACKGROUND

Atom probe tomography has been used for material particle magnification effect and reconstruction into sequence data for a more-detailed study of the metals down to the atomic scale since its first introduction in 1967[1]. It is a three-dimensional material imaging machine with the capability of chemical composition measurements. Compared to other microscopic technique, atom probe tomography offers a spatial solution of sub-0.3 nm scale[5].

2.1 History of Atom Probe

The first atom probe was introduced in 1967 by Erwin Wilhelm Mller and J. A. Panitz during the 14th Field Emission Symposium[1].A field ion microscope was reconfigured by combining the microscope and a Time-of-Flight (ToF) mass spectrometer. With Quartz tubing as the specimen and gimble and stainless steel as the flight tube, John Panitz demonstrated the operation of atom probe with the capability to pulse the electric field on the specimen for atom evaporation, position the atom inside the aperture, and detect the atom as an ion as well as its flight time in one dimension[6, 7]. Figure 2.1 shows the schematic of the first atom probe instrumented by Panitz [8]. The first successful demonstration and public disclosure of atom probe led to a vast growth of related technology. By the end of 1970s, under the leadership of George Smith from University of Oxford, Vacuum Generators debuted the first commercial atom probe. At the same time, Panitz constructed development and introduced the imaging atom probe(IAP), an advancement of 10 cm atom probe [9, 10]. The IAP is the first three-dimensional atom probe and had the ability of detect all the ions of a given specimen at apporaching 100 percent accuracy[11]. On the other hand, a limit had imposed on the IAP with the position sensitivity problem as IAP lacked the ability to

map all the atoms by types at the same time.

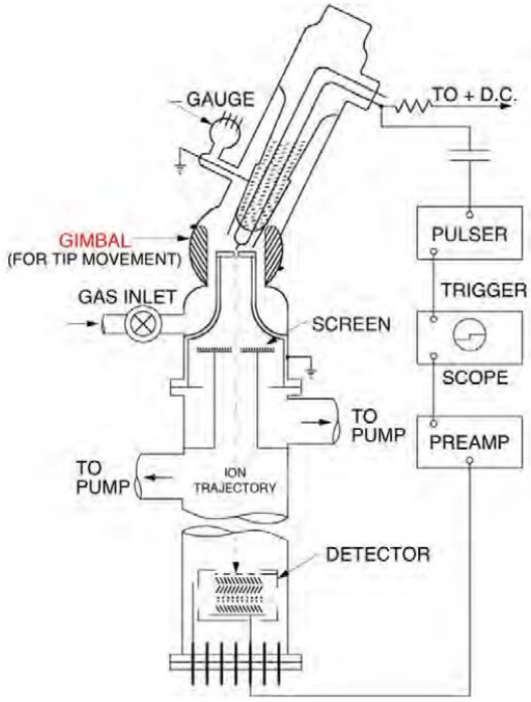

Figure 2.1: Schematic of the first atom probe by Muller and Panitz

2.2 Development of Atom Probe Tomography

In the 1980s, attempts to overcome the limitations of atom probes were made by Alfred Cerezo, Terry Godfrey, and George Smith, who later successfully demonstrated a position-sensitive atom probe in three dimensional space. A position-sensitive detector was installed on an VG APFIM 100 model IAP[12, 13]. Such optimization brought the first imaging of samples in three dimensions with atomic-scale resolution and the instruments was given the name three-dimensional atom probes (3DAP). Soon, a group of scientists at the Universit de Rouen developed a optimized 3DAP and named it tomographic atom probe (TAP)[14, 15].

Over the development of TAP, improvements have been made for optimization purposes such as the image resolution and data generation rate. In 1994, Osamu Nishikwa from Kanazawa Institute of Technology presented a prototype of what was called Scanning

atom probe (SAP)[16, 17], which made possible to analyze sharp atom tip by applying high electric field from an aperture with the shape of hollow cone and collecting the evaporated atoms from a detector. Such optimization improves the images resolution of atoms, as well as the field of view. About the same period, Thomas Kelly from the University of Wisconsin-Madison invented the local electrode atom probe (LEAP) which significantly improved the data collection rate from 1 atom per second to a million atoms per minute. The key improvement behind this instrument was the application of local electrode, as the higher electric field of the electrode made possible to generate higher pulse repetition rates as well as reduce the energy spread of the evaporated ions, resulting in a optimization in image resolution[18, 19]. Figure 2.2 shows a schematic of LEAP[20]. Laser pulsing was later added and led the exploration of analyzing less electrically conductive materials, semiconductors and insulators[21]. Nowadays, LEAP has become the trend in material characterization machinery as LEAP had been commercialized by Kelly and over 100 shipments has been made as of 2017[6].

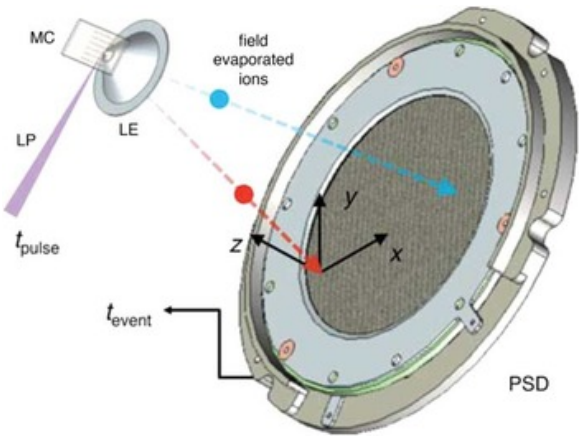

Figure 2.2: Schematic of a local electrode atom probe (LEAP). MC is a microtip coupon, LP is a laser pulse, LE is the local electrode, and PSD is the position-sensitive detector. Reprinted with permission from[20].

2.3 Basic Operation of Atom Probe Tomography

The operation of atom probe tomography requires a sharp specimen tip biased in high electric field, hence high voltage to enable atom evaporation. A DC biasing voltage of 2-10 kV is used in the simulations in this project. A sharp tip helps induces a high electric field at the tip apex under high voltage environment, bring one or more atoms at the point of field evaporation. A laser or HV pulsing helps enable the evaporation of the atom from the specimen surface[22, 23]. Evaporated atom or atoms, now become field ions, are projected through local electrode and onto position-sensitive detector (PSD) of high capturing rate. The collected atom position will be evaluated with the time-of-flight for the element identification. Figure 2.3 shows a schematic of atom probe tomography under HV and illuminated in laser pulsing[24].

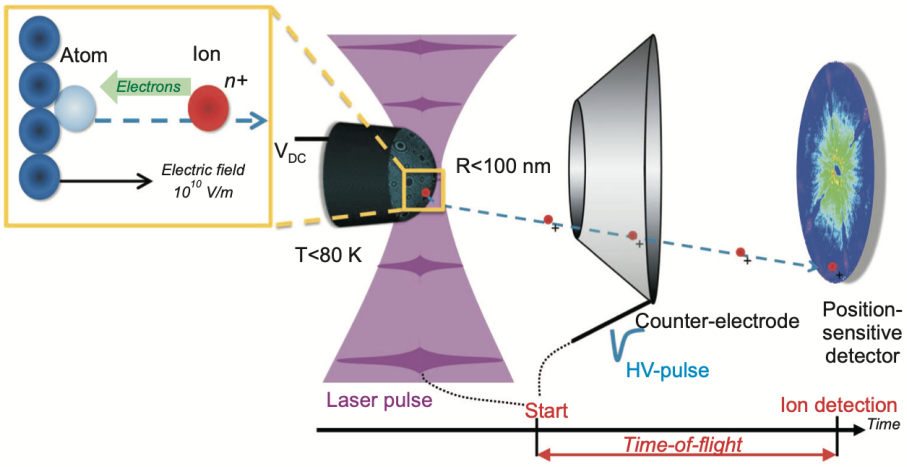

Figure 2.3: Schematic of atom probe tomography with laser pulse in operation. V_{DC} denotes direct current voltage. T denotes temperature.

2.4 Fundamentals of GaN

GaN is a III-V semiconductor with a Wurtzite crystal structure. Commonly used as a violet laser light-emitting diode, GaN has a wide direct bandgap energy of 3.4 eV and high thermal conductivity of 1500 $cm^2/(V \cdot s)$, making it a preferred material in high power

transistor and high frequency devices[25]. The growing use of GaN as the main material of Terahertz (THz) devices and power amplifiers has made a detailed characterization of its nanostructure more prominent[26]. In addition, due to its lattice mismatched property, the design of GaN transistor has become either inefficient or over expensive. Attempts to overcome such issue have been achieved by the deposition of GaN on a biaxially strained thin film or imposing an limit at its critical thickness. The high melting point of GaN also makes the growing of bulk GaN hard, given that materials decomposition becomes highly possible at high temperature. As a result, most GaN devices are grown heteroepitaxially on silicon substrates.

The most widely-used dopant on GaN material to form n-doped GaN is Silicon (Si) [27, 28]. Using Si as dopant brings higher tensile stress and misfit dislocation density, making the compound brittle and lowering the mobility of the device [29]. As a result, most of the Si-doped n-type GaN have a dopant concentration ranging from $5\mathrm{e}16cm^{-3}$ to $7\mathrm{e}18cm^{-3}$ under room temperature [30, 31]. There have been efforts made on growing higher quality GaN device with minimal defects where a GaN film was grown on GaN buffer layer on a sapphire substrate, making a lightly-doped device with high Hall mobility under low temperatures [32].

The nano-structure of GaN has also been studied in atom probe tomography[33]. In order to better understand the fundamentals of APT processes and guide the experimental studies of GaN alloys, the specifications of the project are largely in correlation with the experimental team in NIST. To conduct an APT experiment, temperature as low as $50K$ is required. Under such low temperature, the unintentional doping concentration of GaN can vary from $1\mathrm{e}16cm^{-3}$ to $1\mathrm{e}18cm^{-3}$, a range that we employed in this project.

CHAPTER 3
MATHEMATICAL MODELING

The method of simulating the field and charge behavior of the semiconductor tip under an atom probe tomographic environment is to discretize the overall environment into fine meshing data points and find the electrostatic potential individually at each point. Poisson's equation for electrostatics is a partial differential equation for finding electric potential under a given charge distribution. This chapter details the derivation of Poisson's equation in electrostatics in self-consistent form as well as in discrete matrix operations, methods to find solutions of electrostatic potentials, including box integration method and Newton's method for approximation. In addition, this chapter will display the model of the simulated APT environment, and will introduce the Triangle program useful for triangular meshing and the related command switch.

3.1 Derivation of Poisson's Equations in Electrostatics

Poisson's equation in electrostatics is a derivation from Gauss's Law and the definition of the electrostatic potential in differential form.

The Gauss's law for electricity states the relationship between the electric field and charge density under a enclosed volume V. Equation (3.1) defines electric flux as the fraction of charge Q enclosed by volume V and electric constant ε:

$$\Phi_E = \frac{Q}{\varepsilon} \tag{3.1}$$

In addition, the strength electric flux can be defined as the integral of electric field under a

surface, as equation (3.2) expresses:

$$\Phi_E = \oiint_S \vec{E} dA \tag{3.2}$$

E denotes the electric field from the flux, dA is the differential form of area S. Using Divergence theorem, and defining ρ as the charge density of charge Q under volume V,

$$\rho = \frac{Q}{V} \tag{3.3}$$

the Gauss's law can be expressed in differential form in (3.4).

$$\nabla \cdot \vec{E} = \frac{\rho}{\varepsilon} \tag{3.4}$$

In electrostatics, electric field can be written as the negative divergence of electric potential:

$$\vec{E} = -\nabla \phi \tag{3.5}$$

Combining equation (3.4) and (3.5), the Poisson's equation for electrostatics is derived as the the following,

$$\nabla^2 \cdot \phi(\vec{r}) = -\frac{\rho}{\varepsilon} \tag{3.6}$$

which states that the second-order divergence of electric potential is equal to the negative form of electric charge density within enclosed volume divided by the electric permittivity of the medium within the the enclosed volume.

3.2 Derivation of Self-Consistent Charge Density Equations

A mathematical model for the charge-related behaviors in the atom probe environment is electrons and holes concentrations, which is a set of equations combining the Fermi-Dirac integral and density of states. A modified version of such model is derived given the change

of potential which changes the conduction band and valence bands. Equations (3.7) and (3.8) derives the modified conduction band and valence band based on the potential ϕ:

$$E_C = E_{C,0} - e\phi \tag{3.7}$$

$$E_V = E_{V,0} - e\phi \tag{3.8}$$

where $E_{C,0}$ and $E_{V,0}$ represents the conduction band and valence band at zero biasing voltage and are considered constant depending on the material.

Fermi-Dirac distribution is a probability function that states the probability of a carrier with energy E $f(E)$ is expressed as the following:

$$f(E) = \frac{1}{e^{\frac{E-E_f}{k_b T}} - 1} \tag{3.9}$$

where T denotes temperature and k_b represents the Boltzmann constant which is equal to $1.38 \times 10^{23} m^2 kg/s^2 K$. E_f represents the Fermi energy level referring to the average energy level of carriers in a crystal. The density of states for electrons and holes are the number of energy states for carriers existed per volume per energy level E which depends on the effective mass of carriers in the material and conduction band energy level. The density of states for electrons above the conduction band is:

$$g_C(E) = \frac{m_n^* \sqrt{2m_n^*(E - E_C)}}{\pi^2 \hbar^3}, E \geq E_C. \tag{3.10}$$

The density of states for holes below the valence band is:

$$g_V(E) = \frac{m_p^* \sqrt{2m_p^*(E_V - E)}}{\pi^2 \hbar^3}, E \leq E_V. \tag{3.11}$$

where m_n^* and m_p^* denotes the effective mass of electrons and holes. To calculate the carrier

concentrations for electrons and holes, the solution is to integrate the combinations of the density of states for carriers and Fermi distribution function with respect to energy E and under the endpoints of conduction band ranges and valence band respectively, as follow:

$$n = \int_{E_C}^{+\infty} f(E) g_C(E) dE = \frac{m_n^* \sqrt{2m_n^*}}{\pi^2 \hbar^3} \int_{E_C}^{+\infty} \frac{\sqrt{E - E_C}}{1 + e^{(E-E_f)/k_b T}} dE \tag{3.12}$$

$$p = \int_{-\infty}^{E_V} f(E) g_V(E) dE = \frac{m_p^* \sqrt{2m_p^*}}{\pi^2 \hbar^3} \int_{-\infty}^{E_V} \frac{\sqrt{E_V - E}}{1 + e^{(E-E_f)/k_b T}} dE \tag{3.13}$$

Plugging the conduction and valence band energy levels developed in (3.7) and (3.8), the mobile electrons and holes concentrations at each energy level E becomes dependent on the charge potential ϕ as well, as the equation set shows below:

$$n(\phi) = \frac{m_n^* \sqrt{2m_n^*}}{\pi^2 \hbar^3} \int_{E_{C,0} - e\phi}^{+\infty} \frac{\sqrt{E - E_C(\phi)}}{1 + e^{(E-E_f)/k_b T}} dE \tag{3.14}$$

$$p(\phi) = \frac{m_p^* \sqrt{2m_p^*}}{\pi^2 \hbar^3} \int_{-\infty}^{E_{V,0} - e\phi} \frac{\sqrt{E_V(\phi) - E}}{1 + e^{(E-E_f)/k_b T}} dE \tag{3.15}$$

To link the Poisson's equations and carrier concentration equations together, we need to find the relationship between charge density and carrier concentrations. Under a nonzero biasing voltage, the net charge density of a semiconductor material is as follows,

$$\rho_v = e(N_D^+ - N_A^- + p - n) \tag{3.16}$$

where N_D^+ denotes the concentration of ionized donors and N_A^- denotes the concentration of ionized acceptors in the doped semiconductor. If assumptions to be made on a total ionization of dopants in the semiconductor, equation (3.16) now becomes:

$$\rho_v = e(N_D - N_A + p - n), \tag{3.17}$$

and N_D and N_A are the dopant concentrations initially injected into the semiconductor tip. Furthermore, the majority of this simulation is ran on a n-type doping semiconductor tip, the N_A term is neglected, combing with the mobile carrier concentrations, the charge density becomes:

$$\begin{aligned}\frac{\rho_v}{e} &= N_D + p - n \\ &= N_D + \frac{m_p^*\sqrt{2m_p^*}}{\pi^2\hbar^3}\int_{-\infty}^{E_{V,0}-e\phi}\frac{\sqrt{E_V(\phi)-E}}{1+e^{(E-E_f)/k_bT}}dE \\ &- \frac{m_n^*\sqrt{2m_n^*}}{\pi^2\hbar^3}\int_{E_{C,0}-e\phi}^{+\infty}\frac{\sqrt{E-E_C(\phi)}}{1+e^{(E-E_f)/k_bT}}dE\end{aligned} \tag{3.18}$$

Substituting the charge density ρ_v with the Poisson's equation for electrostatics in equation (3.6), a full self-consistent charge density equation depending on the electrostatic potential is derived as:

$$\begin{aligned}\frac{\varepsilon}{e}(\nabla^2\cdot\phi) = N_D + \frac{m_p^*\sqrt{2m_p^*}}{\pi^2\hbar^3}\int_{-\infty}^{E_{V,0}-e\phi}\frac{\sqrt{E_V(\phi)-E}}{1+e^{(E-E_f)/k_bT}}dE \\ - \frac{m_n^*\sqrt{2m_n^*}}{\pi^2\hbar^3}\int_{E_{C,0}-e\phi}^{+\infty}\frac{\sqrt{E-E_C(\phi)}}{1+e^{(E-E_f)/k_bT}}dE.\end{aligned} \tag{3.19}$$

3.3 Discretizing Poisson's Equations

In section 3.1 a model was derived for solving for Poisson's equations under an APT environment. The equations are derived under the continuous cases which will be taken further into discrete cases in simulation. This section explains the further processing of Poisson's equations, including constructing discrete matrices and Newton's method for approximation, to derive the simulation model.

3.3.1 Constructing the Poisson Matrix

The construction of Poisson Matrix is mainly based on the Voronoi diagram and the node points, which are both outputs from the meshed models. Voronoi diagram The method to discretize the environment is based on the box integration method. A Voronoi diagram is a mathematical plane partitioning technique named after Russian mathematician Georgy Voronoy. In a Voronoi diagram, each node would have an assigned partition of a plane closer to that node than any other. As the meshed model contains thousands of nodes along with tens of thousands of edges, a good way to view the discretized model is to start with a simple model. Assume node points are formed as a combination of meshed triangle edges. A example Voronoi diagram is made surrounding the node $P3$ labeled in dashed line, as it shows in figure 3.1. Label the triangle edges as'd's, and Voronoi edges with 'l's. It's clearly shown that the Voronoi edges and triangle edges have dissected the Voronoi areas into four boxes. Label these boxes with 'A's along with subscripts and the triangles formed with straight lines with 'T's, as it is shown in figure 3.8. Assuming in each triangle T, charge density ρ and electron permittivity ε are constant within the labeled triangle, label them with the corresponding number.

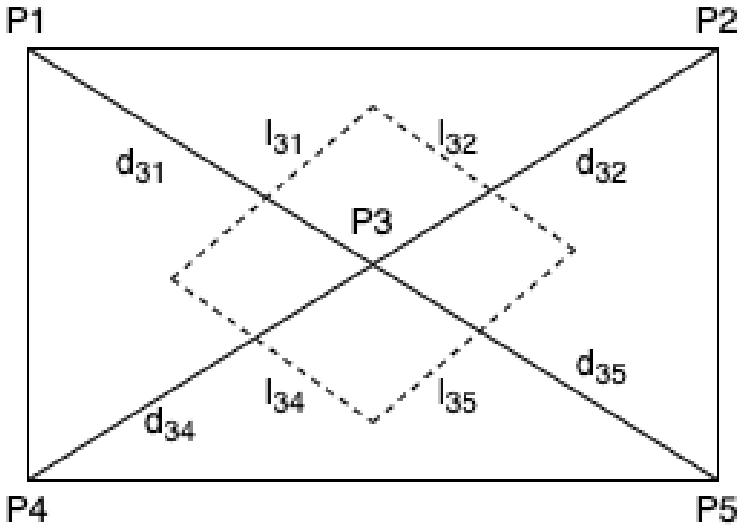

Figure 3.1: A Voronoi diagram surrounding node P3

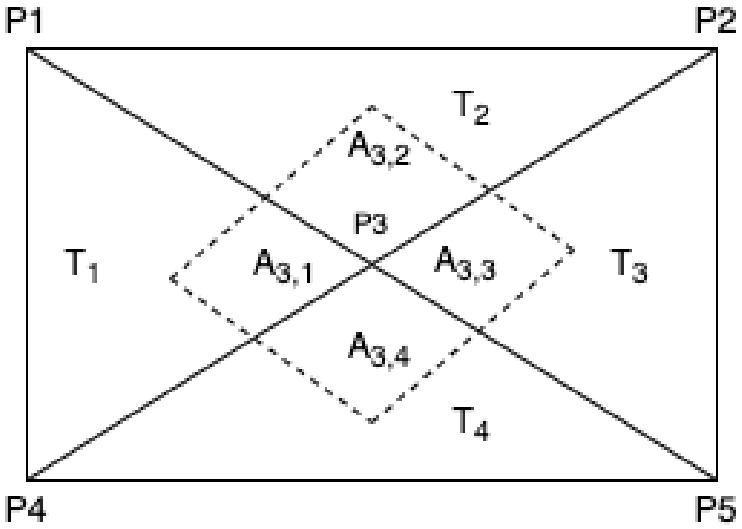

Figure 3.2: Labeled Voronoi boxes surrounding node P3

Here, node $P3$ is surrounded by four Voronoi boxes. The next step is to integrate Poisson's equation on node $P3$ with the following equation:

$$\iint_{V_3} \varepsilon \nabla^2 \cdot \phi dxdy = -\iint_{V_3} \rho dxdy \tag{3.20}$$

where V_3 denotes the Voronoi area surrounding node $P3$. The right-hand side of the equation is easily interpreted as the total charge in the Voronoi area surrounding P3, which is the summation of total charge in the dashed Voronoi boxes, as shown below:

$$\begin{aligned} RHS &= -\iint_{V_3} \rho dxdy \\ &= -(\rho_1 A_{3,1} + \rho_2 A_{3,2} + \rho_3 A_{3,3} + \rho_4 A_{3,4}) \\ &= -\sum_j \rho_j A_{3,j} \end{aligned} \tag{3.21}$$

the left-hand side of equation 3.20 can be simplified using the divergence theorem as

shown: can be simplified as the following:

$$\begin{aligned} LHS &= \iint_{V_3} \varepsilon \nabla^2 \cdot \phi dx dy \\ &= \int_{perimeter_l} \hat{n_3} \cdot \varepsilon \nabla \phi dl \end{aligned} \tag{3.22}$$

where $\hat{n_3}$ represents the normal vector pointing outward of the Voronoi diagram surrounding node $P3$, and the double integral can be turned into single integral over the Voronoi box edges. Given that every edge of each Voronoi boxes is small, the value of $\nabla\phi$ can be approximated as a constant along each triangle edge. Using this approximation, equation 3.22 can be taken further as:

$$\begin{aligned} LHS &= \int_{perimeter_l} \hat{n_3} \cdot \varepsilon \nabla \phi dl \\ &= (l_{32,3}\,\varepsilon_3 + l_{32,2}\,\varepsilon_2)(\frac{\phi_2 - \phi_3}{d_{32}}) \\ &+ (l_{35,3}\,\varepsilon_3 + l_{35,5}\,\varepsilon_5)(\frac{\phi_5 - \phi_3}{d_{35}}) \\ &+ (l_{31,3}\,\varepsilon_3 + l_{31,1}\,\varepsilon_1)(\frac{\phi_1 - \phi_3}{d_{31}}) \\ &+ (l_{34,3}\,\varepsilon_3 + l_{34,4}\,\varepsilon_4)(\frac{\phi_4 - \phi_3}{d_{34}}) \end{aligned} \tag{3.23}$$

where $l_{ij,k}$ in the equation denotes the dividend of Voronoi edge l_{ij} locating in the kth triangle. Combining the left-hand side with right-hand side, the full discrete Poisson's equation for Voronoi diagram surrounding node $P3$ is:

$$\begin{aligned} -\sum_j \rho_j A_{3,j} =& (l_{32,3}\,\varepsilon_3 + l_{32,2}\,\varepsilon_2)(\frac{\phi_2 - \phi_3}{d_{32}}) \\ &+ (l_{35,3}\,\varepsilon_3 + l_{35,5}\,\varepsilon_5)(\frac{\phi_5 - \phi_3}{d_{35}}) \\ &+ (l_{31,3}\,\varepsilon_3 + l_{31,1}\,\varepsilon_1)(\frac{\phi_1 - \phi_3}{d_{31}}) \\ &+ (l_{34,3}\,\varepsilon_3 + l_{34,4}\,\varepsilon_4)(\frac{\phi_4 - \phi_3}{d_{34}}) \end{aligned} \tag{3.24}$$

By doing such discrete integration to other nodes with their own Voronoi diagram, a matrix can be assembled under the potential ϕ and charge density ρ:

$$\begin{bmatrix} M_{11} & M_{12} & M_{13} & M_{14} & M_{15} \\ M_{21} & M_{22} & M_{23} & M_{24} & M_{25} \\ M_{31} & M_{32} & M_{33} & M_{34} & M_{35} \\ M_{41} & M_{42} & M_{43} & M_{44} & M_{45} \\ M_{51} & M_{52} & M_{53} & M_{54} & M_{55} \end{bmatrix} \begin{bmatrix} \phi_1 \\ \phi_2 \\ \phi_3 \\ \phi_4 \\ \phi_5 \end{bmatrix} = \begin{bmatrix} -\sum_j \rho_j A_{1,j} \\ -\sum_j \rho_j A_{2,j} \\ -\sum_j \rho_j A_{3,j} \\ -\sum_j \rho_j A_{4,j} \\ -\sum_j \rho_j A_{5,j} \end{bmatrix} \tag{3.25}$$

where the 3rd row of the matrix is re-organized from equation 3.24 as such:

$$\begin{aligned} M_{31} &= (l_{31,3}\,\varepsilon_3 + l_{31,1}\,\varepsilon_1)\frac{1}{d_{31}} \\ M_{32} &= (l_{32,3}\,\varepsilon_3 + l_{32,2}\,\varepsilon_2)\frac{1}{d_{32}} \\ M_{34} &= (l_{34,3}\,\varepsilon_3 + l_{34,4}\,\varepsilon_4)\frac{1}{d_{34}} \\ M_{35} &= (l_{35,3}\,\varepsilon_3 + l_{35,5}\,\varepsilon_5)\frac{1}{d_{35}} \\ M_{33} &= -(M_{31} + M_{32} + M_{34} + M_{35}) \\ \sum_j \rho_j A_{3,j} &= (\rho_1 A_{3,1} + \rho_2 A_{3,2} + \rho_3 A_{3,3} + \rho_4 A_{3,4}) \end{aligned} \tag{3.26}$$

The next step is to find the relation between electric potential ϕ and charge density ρ. Recall in section 3.2, the equation for density ρ for a semiconductor is provided in equation 3.17. The calculation of n for a semiconductor under doping can be rewritten as:

$$n = N_c \frac{2}{\sqrt{\pi}} F_{1/2}(\eta_c) \tag{3.27}$$

where N_c denotes the effective density of states in the conduction band and is defined as:

$$N_c = 2[\frac{m_n^*(kT)}{2\pi\hbar^2}]^{3/2} \tag{3.28}$$

the term $F_{1/2}(\eta_c)$ denotes the Fermi-dirac integral of order $1/2$ at η_c:

$$F_{1/2}(\eta_c) = \int_0^\infty \frac{\eta^{1/2}}{1 + e^{(\eta - \eta_c)}} d\eta \tag{3.29}$$

where,

$$\eta_c = \frac{(E_F - E_C)}{kT} \tag{3.30}$$

Note that the Fermi-dirac integral can be numerically calculated or traced from tables. Recall from equation 3.7, conduction band can be derived from potential ϕ, equation 3.30 can be rewritten as:

$$\begin{aligned} \eta_c &= \frac{E_F - (E_{C,0} - e\phi)}{kT} \\ &= \frac{(E_F - E_{C,0})}{kT} + \frac{e\phi}{kT} \\ &= \eta_{c,0} + \frac{e\phi}{kT} \end{aligned} \tag{3.31}$$

Same for p, it can be derived as:

$$p = N_v \frac{2}{\sqrt{\pi}} F_{1/2}(\eta_v) \tag{3.32}$$

where N_v is effective density of states in the valence band and η_v becomes:

$$\begin{aligned} \eta_v &= \frac{((E_{V,0} - e\phi) - E_F)}{kT} \\ &= \eta_{v,0} - \frac{e\phi}{kT} \end{aligned} \tag{3.33}$$

Now charge density ρ can be rewritten as a function of ϕ, denoted as $\rho_i = q(\phi_i)$.

3.3.2 Newton's Method for Approximation

The previous section explained the construction of a matrix equation which represents the discretized Poissons equation. Using the same explanations developed in equation 3.25, a

set of matrices equation can be developed for the 3D APT environment:

$$\mathbb{A} \cdot \phi = -\mathbb{Q}(\phi) \tag{3.34}$$

where $\mathbb{A}$ denotes the coefficients of Voronoi boxes under the environment, and $\mathbb{Q}(\phi)$ denotes a voltage-dependent matrix. The goal of setting this equation is to solve the potential matrix ϕ using matrix calculation. Rewrite it as:

$$\mathbb{A} \cdot \phi + \mathbb{I} \cdot \mathbb{Q}(\phi) = 0 \tag{3.35}$$

$\mathbb{I}$ denotes the identity matrix.

Given that every element the matrix is a real value element, it's not possible to find the exact solution to solve for matrix ϕ, therefore, Newton's method is then used to find an approximate solution as close to 0 as possible. Newtons method requires an initial guess for ϕ, which we commonly take to be zero everywhere. This is possible because under any biasing condition zero potential at every point is not realistic. Denote the initial guess as $\phi_{i,1} = 0$, for every existing node i in the environment. Define a residual matrix $\mathbb{R}_m$ as follows:

$$\begin{aligned} \mathbb{R}_m &= \mathbb{A} \cdot \phi_m + \mathbb{I} \cdot \mathbb{Q}(\phi_m) \\ &= \mathbb{F}(\phi_m) \end{aligned} \tag{3.36}$$

where subscript m denotes the mth runs of the program. Define $\mathbb{J}$ as the Jacobian matrix, a first order partial derivative matrix, where a general entry of such is:

$$\mathbb{J}_{ij} = \frac{\partial \mathbb{F}_i}{\partial \phi_j} \tag{3.37}$$

For the solution of the Poisson matrix, the Jacobian matrix is written as:

$$\mathbb{J}_m = \mathbb{A} + \mathbb{Q}'(\phi_m) \tag{3.38}$$

At any boundary condition and for oxide materials, $\mathbb{Q}'(\phi_m) = 0$. For semiconductor material, the calculation involves the derivative of charge density which is:

$$\begin{aligned} \rho' &= \frac{\partial[e(N_D - N_A + p - n)]}{\partial\phi} \\ &= e(p' - n') \\ &= \frac{e}{kT}[N_V F_{-1/2}(\eta_v(\phi)) - N_C F_{-1/2}(\eta_c(\phi))] \end{aligned} \tag{3.39}$$

where $F_{-1/2}(\eta)$ is the derivative of Fermi-dirac function and like the general Fermi-dirac function, the value can be calculated numerically with the corresponding η. With the equation above, the Jacobian matrix can be expressed as:

$$\mathbb{J} = \mathbb{A} + \frac{\rho' \cdot V(n)}{\varepsilon} \tag{3.40}$$

where $V(n)$ denotes the area of the 2D Voronoi diagram of node n. With the Jacobian matrix $\mathbb{J}$ and the residual matrix $\mathbb{R}$, the relationship below:

$$\mathbb{R}_m + \mathbb{J}_m(\phi_m)\Delta_m = 0 \tag{3.41}$$

is useful for updating a new estimation for potential matrix ϕ_{m+1} where

$$\phi_{m+1} = \phi_m + \Delta_m \tag{3.42}$$

The differential matrix Δ can be calculated from rearranging equation (3.41),

$$\Delta_m = -\{\mathbb{J}_m\}^{-1} \cdot \mathbb{R}_m \tag{3.43}$$

The updated potential ϕ_{m+1} will then be fed into the operator $\mathbb{F}$ to calculate the new residual matrix $\mathbb{R}_{m+1}$ and new Jacobian matrix $\mathbb{J}_{m+1}$. By repeating this process, every element from the residual matrix $\mathbb{R}$ will get closer to zero each time. While it still seems unlikely to reach the point such that $\mathbb{R}_i = 0$ for every node i in the model, a upper threshold can be set such that once the maximum element from the residual $\mathbb{R}$ drops below the threshold, the program can be prompted to stop and we can say the results of potential ϕ is a reasonable solution for the problem. In this project, the thresholds set for low standard voltage and high standard voltage are as follows:

$$\max(\mathbb{R}_i) \leq 1\text{e}{-16}, \quad \text{for low contact voltages} \tag{3.44}$$

$$\max(\mathbb{R}_i) \leq 1\text{e}{-6}, \quad \text{for high contact voltages} \tag{3.45}$$

Using a reasonable threshold can provide the best possible solution ϕ_i while keeping run time of the program at a reasonable pace.

3.4 APT Environment and Triangular Meshing

This section introduces the constructed 3D cylindrical environment of the APT and the specific boundary conditions surrounding the environment. Later it will also cover the background on the two-dimensional triangular mesh generation program 'Triangle' and specify how to obtain an acceptable mesh. The code can simulate either a 3D cylindrically symmetric (no ϕ variation) or 2D planar model. A 3D cylindrical model has been used for most simulations for the following reasons: 1) The samples we are simulating are cylindrically symmetric, and we wish to calculate the field and charge surrounding the probe tip; the cylindrically symmetric model is therefore more accurate and appropriate for our problem. 2) One of the shortcomings of using a 3D cylindrical model is that the model is unable to accurately simulate effects such as spontaneous polarization within the GaN

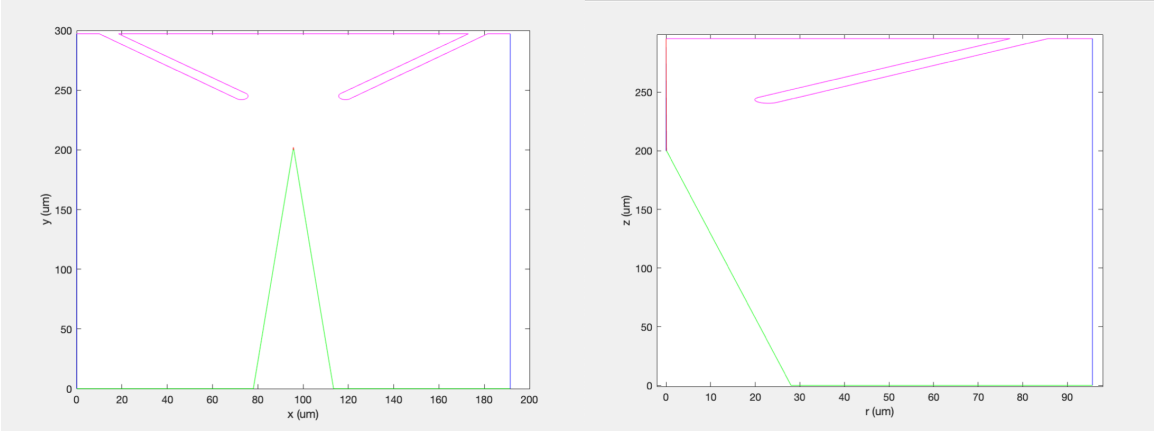

Figure 3.3: 2D planar modeling (on the left) and 3D Cylindrical modeling (on the right) of an APT environment in simulation.

tip, which is not cylindrically symmetric. However, given that APT usually operates in high voltage biasing, the effect of spontaneous polarization on field- and charge behaviors is small compared to the effect under high voltages, therefore, 3D cylindrical model neglecting spontaneous polarization is not important in this case. Figure 3.3 shows examples of 2D planar modeling and 3D cylindrical modeling of APT at the same specifications in comparison. Under the same scale, 3D cylindrical model occupies about a half in geometric area compared to the 2D cylindrical model, which works in benefits when taken into mesh generator, can offer a finer quality mesh.

3.4.1 Modeling Atom Tip

Overall, the APT environment is a combination of three parts: probe tip, a bottom layer boundary, and a top layer boundary. The probe tip in reality is supposed to be an extremely thin conical tip at a scale of a few nanometers. In order to re-create it in the simulation environment as precisely as possible, the tip was modeled as a semicircle with a specific expansion. In the experiment, 20 nanometer-in-radius semicircle tip and 5 degree expansion angle are employed as a standard design. Figure 3.4 shows a half-tip area in a 3D cylindrical model, containing a quarter-circle under careful modeling and the expansion angle.

Further specification of the tip includes the total length of the tip, which is defined as 2 microns at a 5 degree expansion angle. Figure 3.5 shows the half tip of 2 microns in length presented in the 3D cylindrical model.

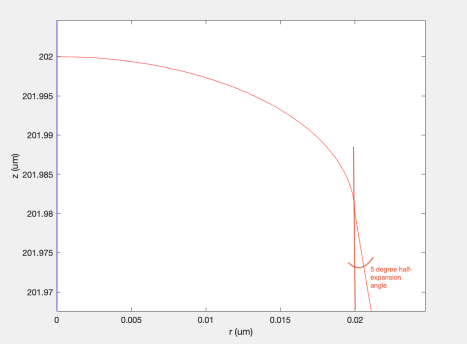

Figure 3.4: Zoom-in area of the half atom tip in 3D cylindrical model

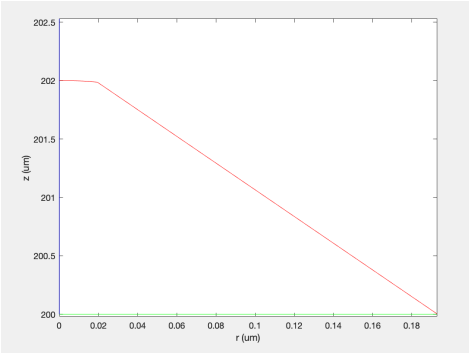

Figure 3.5: Overview of Half Atom Tip in 3D cylindrical model

3.4.2 Local Electrode Modeling

The local electrode has become an essential part to form a L-APT since it provides a better solution for capturing separated atom without destroying it. The aim to model the local electrode in simulation is to reconstruct it as precisely and accurately as possible. As a result, the local electrode is modeled as a conical shaped tube tilted at an angle to form an aperture. The specification of the electrode includes the radius of the electrode, the length, and its tilted angle relative to the coaxial apex. Over the course of the project, all three parameters have been held constant: the diameter of electrode is 6 microns, overall length is 50 microns, the tilted angle is 45 degrees. The local electrode is placed from 20 microns away from the tip in parallel axis and 40 microns in vertical axis. Figure 3.6 shows the shape of the local electrode in model.

3.4.3 Defining Boundary Conditions

Given a highly detailed geometry of the cross-sectional view of APT, in preparation for the later step of generating a successful mesh, boundaries are defined in terms of different

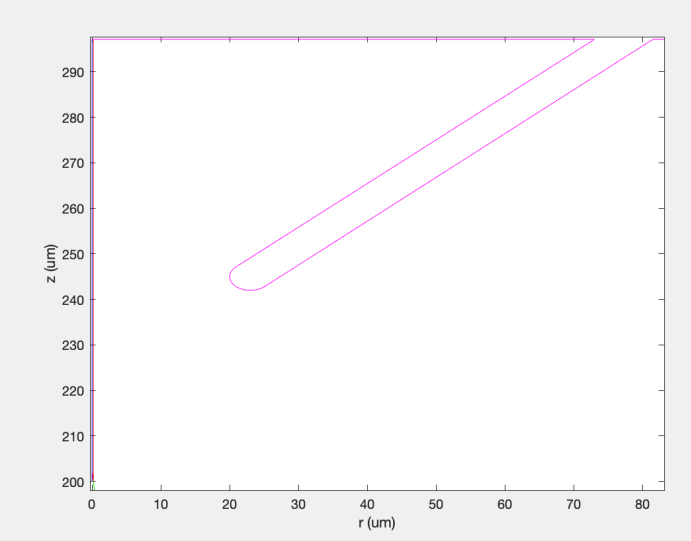

Figure 3.6: Local Electrode in 3D Cylindrical Model

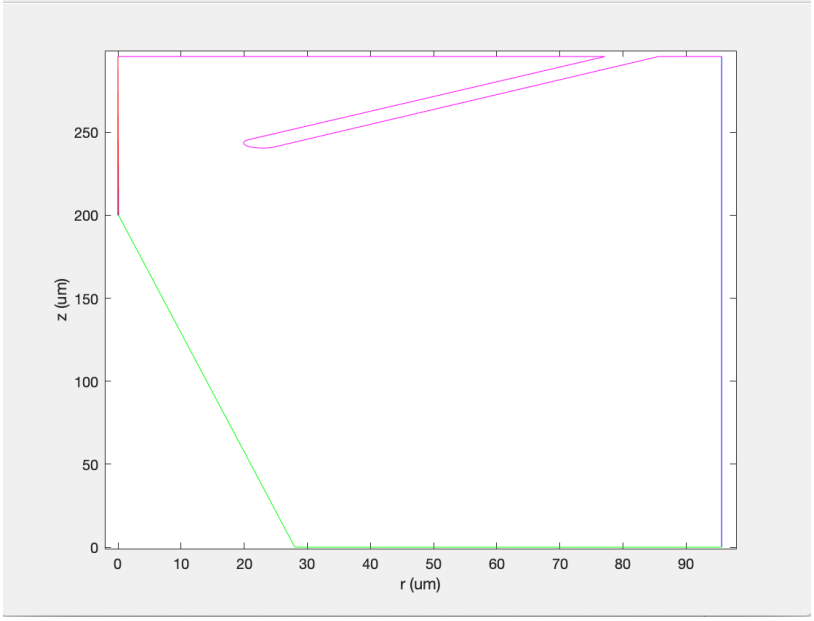

Figure 3.7: Cross-sectional View of 3D Cylindrical Symmetric Model of APT, including different types of boundaries represented in different colors. Lines with marker values 0 are represented in red; Lines with marker values 1 are represented in blue; Lines with marker value 2 are represented in green; Lines with marker value 3 are represented in magenta.

marker numbers, which represents different boundary conditions in discrete calculations. Every line defined in the model must have a corresponding marker values. The boundary markers are defined as follows: Lines that are not classified as a boundary are assigned marker 0. In the project, any line that are within the APT environment are assigned 0. Lines

that are used as a symmetrical axis are defined as Neumann boundary and assigned marker value of 1. The left and right vertical axial lines in the environment are the symmetrical axis, therefore are the Neumann boundary. Bottom contact is, by material, composed of heavily-doped Poly-Silicon, where it can be treated as a metal contact. Top contact consists of local electrode, which is defined as a metal contact. Both Top and bottom contacts are used as a biasing contacts, where voltages will be applied on, therefore, top and bottom contacts meets the Dirichlet boundary conditions, where each node are held at a fixed voltage. The bottom contact is assigned marker value 2, while the top contact is assigned with marker value 3. The boundary markers are written in the following the format from the Triangle program,

$<$ Edge number $><$ endpoint 1 $><$ endpoint 2 $><$ Boundary Marker number $>$

Where the two endpoints represent the numbered points defined previously. To present the APT environment in figure, different colors are used to represent different marker values, providing a clearer view of the cross-sectional environment. Figure 3.7 shows the whole environment, including boundaries represented by different colors, of a cross-sectional view of 3D cylindrical symmetric model of APT in simulation.

3.4.4 Material Definition

Regions enclosed entirely within the simulation domain (surrounded by segments) are assigned material attributes. Regional attributes are used in the code to define different materials. In the project, the area surrounded by tip boundary is set as semiconductor, while the rest of the area is set as air. To differentiate the two areas, regional attribute marker '1' is used for GaN region, also known as the tip, regional attribute marker '2' is used for air. The regional markers are written in the following form to follow the Triangle program meshing guideline:

$<$ Region number $><$ x coordinate $><$ y coordinate $><$ regional attribute $>$

where x coordinate and y coordinate refers to any of points within the confined area. Figure

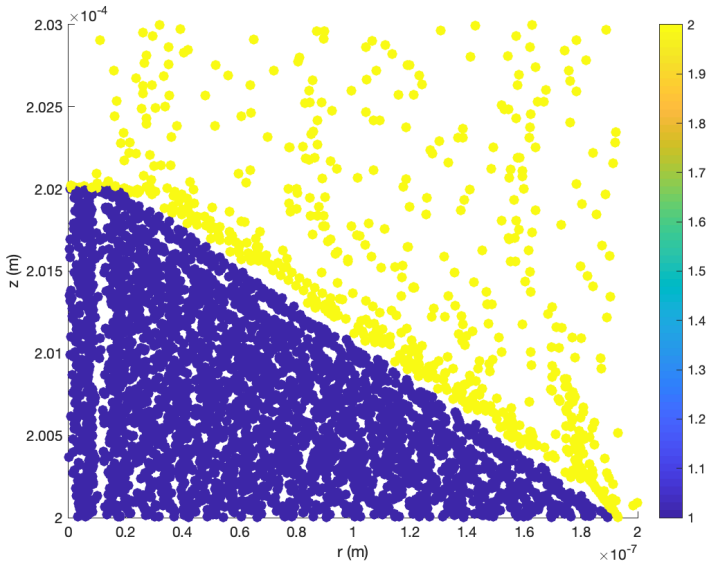

Figure 3.8: Regional attributes on nodes of area surrounding the tip. Color blue denotes regional marker 1 and semiconductor material; Color yellow denotes regional marker 2 and air.

3.8 shows a zoom-in area of nodes of regional attributes, represented by different color, around the tip area.

3.4.5 Triangle Program for Meshing

In this project, all triangular meshing have been done on the 'Triangle' program. Created by Professor J.R Shewchuk in the computer science department of University of California at Berkeley in 2003, Triangle is a quality mesh generating tool that bears the capabilities of generating Delaunay triangle meshes as well as Voronoi diagrams at a fast speed. Operated in different command switches, the program can provides meshes serving requirements such as triangulating a planar straight line graph(PSLG), constraining maximum area of triangular mesh, and forming Voronoi diagrams respectively or simultaneously[3, 4]. By transferring the developed model shown before into a text-representing-graph PSLG file('.poly' file), meshes will be generated in the forms of text files consisting of a finer, more-detailed PSLG ('.poly') file, a '.node' file with the coordinate information on each node formed after execution, and a '.ele' file containing numbered nodes of each numbered

triangle. The following sections introduces the essential command switches used in this project.

-p Command Switch

'-p' switch in the command prompts the program to find and read the PSLG file in the folder and perform a constrained triangular meshing fitted by the model in the PSLG file. In the project, '-p' switch is accompanied by the '-D' switch which so that every triangle formed will be conforming to Delaunay triangulation.

-D Command Switch

As mentioned previously, '-D' switch makes sure the meshed triangle follows the conforming Delaunay triangulation. Delaunay triangulation is a computational mathematics method which states that none of the nodes in a given set of coordinates will lie within any circumscribed circle of a triangle formed in the triangulation process[34]. The use of Delaunay triangulation would substantially avoid the probability of overlapping triangles.

-a Command Switch

'-a' switch imposes a maximum limit on the area of a triangle in a confined area. This command is beneficial in the model as it gives flexibility to define the mesh fineness in different regions. As the regions surrounding the the atom tip are more desired so they need to be meshed more finely. Regions outside of the designated area were be meshed at a moderately coarse scale to free up space. In the project, region within the atom tip was meshed with triangles no larger than $1\mathrm{e}{-5}\mu m^2$, where regions outside of the atom tip were meshed at a scale of $10\mu m^2$. A virtual region surrounding the tip has also been made and meshed at a scale of $1\mathrm{e}{-3}\mu m^2$ in order to provide a clearer result and analysis surrounding the atom tip.

-v Command Switch

Using '-v' switch would have the program generate a Voronoi diagram of each meshed-generated node in the file. By using such command, a new set of vertices is outputted partitioning the model into polygonal regions.

3.4.6 Meshed Model

A meshed model done by Triangle showing the 3D cylindrical symmetric model of cross-sectional view of APT is displayed in figure 3.9 [3, 4]. The lists of figures are shown in its original form, meshed figure with meshed triangles, updated nodes with vertices, and confined plane with updated nodes. The model is shown at a different scale.

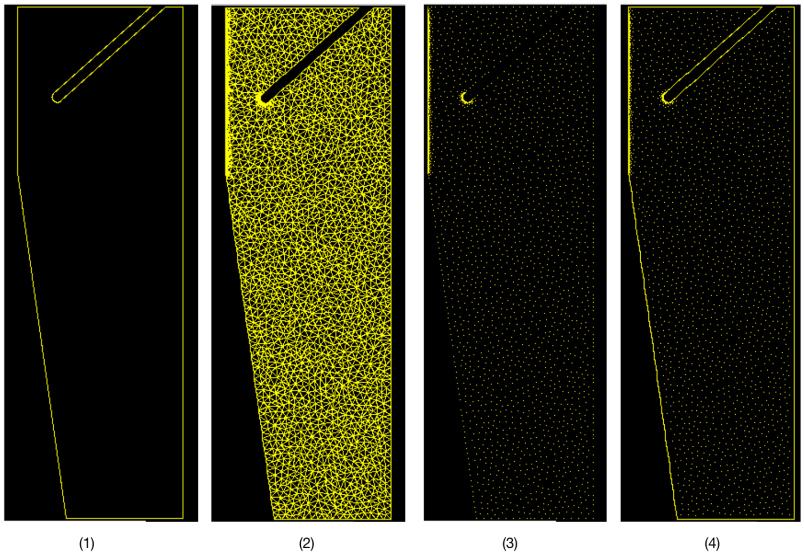

Figure 3.9: Figures Showing Meshed Results after Executing Triangle Program. Figure (1) is the model before meshing; Figure (2) shows the model after meshing; Figure (3) displays all the nodes/vertices; Figure (4) displays the nodes under the boundary edges.

3.5 Data Processing

This section explains how to extract results when the Newton iterations of the discrete Poisson equation have successfully completed. With a successful run of the program, outputs

of electrostatic potential, fixed charge, mobile charge of every node in the model will be saved in the form of double arrays. From these, static electric field, fixed charge density, mobile charge density, and more can be calculated anywhere, or along particular axes.

3.5.1 Net Fixed Charge Density

The calculation of fixed charge density is straightforward. It is clear that there is no charge in the air region. In the semiconductor region (in this project, GaN), since the fixed charge depends on the net uniform doping concentration, the fixed charge density should be uniform within the GaN region as well. Under an n type uniform doping, the fixed charge density for every node in the GaN region follows such equation:

$$\rho_{GaN,fixed} = e \cdot N_D \tag{3.46}$$

3.5.2 Net Mobile Charge Density

The calculation of mobile charge density is similar to that of fixed charge density. Under biasing, both mobile electron and mobile hole concentration will be encountered for net mobile charge density. Again, zero mobile charge density is expected for every node in the air region. In the GaN region, the mobile charge density for the nodes in the GaN region is calculated as:

$$\begin{aligned} \rho_{GaN,mobile} &= e \cdot (p - n) \\ &= e \cdot \{N_v \frac{2}{\sqrt{\pi}} F_{1/2}(\eta_v) - N_c \frac{2}{\sqrt{\pi}} F_{1/2}(\eta_c)\} \end{aligned} \tag{3.47}$$

3.5.3 Axial Electric Field

Electric field is a desired property to be studied in this project. In particular, the electric field in along the symmetric rotating axis (where in the model, r=0) is desired and found. Finding the electrostatic potential on every node lying on the on-z-axis position, the magnitude of

discrete electric field can be calculated using the following equation:

$$E_{i,on-axis} = -\frac{\phi_{i+1} - \phi_i}{\Delta z} \tag{3.48}$$

where Δz denotes the distance between node i and $i + 1$.

3.5.4 K-factor Calculation

In previous work, a simplified analytical model was used to find the peak electric field typically occured near the apex of metallic APT specimens [35, 36]. For a sharp tip with radius r, under a contact voltage difference V, the electric field at the apex E_{apex} was approximated as following:

$$E_{apex} = \frac{V}{k \cdot r} \tag{3.49}$$

where k is a fitting factor which fell in the range 1.5–8.5 for sharp metallic conductors[37, 38]. The k-factor was approximately constant with respect to applied voltage. Further detail regarding the k factor will be explained in Chapter 4.

CHAPTER 4
RESULTS AND ANALYSIS

This chapter shows the simulation results, primarily the electric field along the axis of the sample tip, and the charge density inside the sample tip, in order to understand the behavior of the sample inside the APT environment. This will include analysis of how n-doped GaN behaves similar to metallic materials. The results include GaN samples under low and high voltages. In order to isolate the impact of the charge carriers, a non-physical insulating GaN sample was simulated and the results compared to the n-doped GaN sample.

4.1 GaN Tip under High Contact Voltages

High contact voltages of 2000V, 4000V, 6000V, 8000V, 10000V are the first to be explored given that real-life Atom probe tomography takes place in high voltages. To prepare for the simulation, a $20nm$ radius, $2\mu m$ length GaN tip was used at a n-type doping concentration of $1\text{e}16cm^{-3}$. Shown below at figure 4.1 is a axial electric field along the rotational z-axis at a voltage difference of 2000V. It's clearly shown that at the apex of the tip (at $z = 2.02 \times 10^{-4}m$), electric field magnitude reaches a maximum at $2.414\text{e}{+10}V/m$. It is expected that the peak electric field will occur adjacent to the apex of the tip, as conducting tips commonly have the effect of concentrating electric fields. The k-factor is calculated using equation (3.46) and the above results to be $k = 4.1425$. This result falls in the range of $1.5 < k < 8.5$ which has been found for sharp metal tip samples subjected to atom probe tomography[37]. To verify its validity, more high contact voltages are run under such condition. Table 4.1 shows the simulated k-factor for a vareity of applied voltages. All five calculated k factors are within the range applicable to metallic tips. These results raise the question of why an n-doped GaN tip behaves similarly to metallic tips in APT. To further investigate this problem, a scatter plot of mobile charges around the tip area

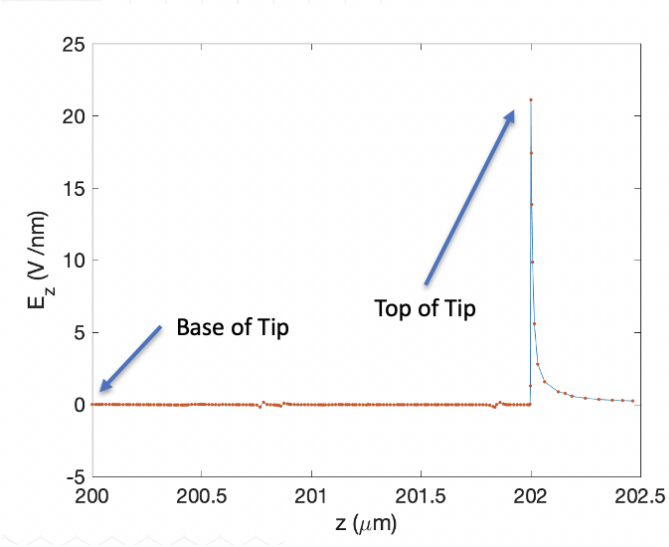

Figure 4.1: Axial Electric field at 2000V contact voltage (Tip radii $r = 20nm$).

Table 4.1: Table of voltages, electric field, and k-factor of 20-nm radii GaN tip at n-type doping concentration of $1\text{e}16cm^{-3}$.

Contact Voltages[kV]	Apex Electric Field[$\times 10^{10}$ V/m]	k-factor
2	2.414	4.1425
4	4.843	4.1297
6	7.271	4.1258
8	9.699	4.1240
10	12.13	4.1230

was created and shown below at figure 4.2. The behavior of the mobile charges around the tip area show an inversion layer of holes (in yellow) near the surface, backed by a depletion region (in green) covering most of the rest of the tip. Under high voltages, it is logical that the layer of electrons and negative charges generated by polarization has been depleted and even inverted. To verify the validity of the phenomenon, more scenarios should be considered by varying one parameter of the model at a time. Section 4.1.1 and 4.1.2 explores two important parameter change regarding to the original model.

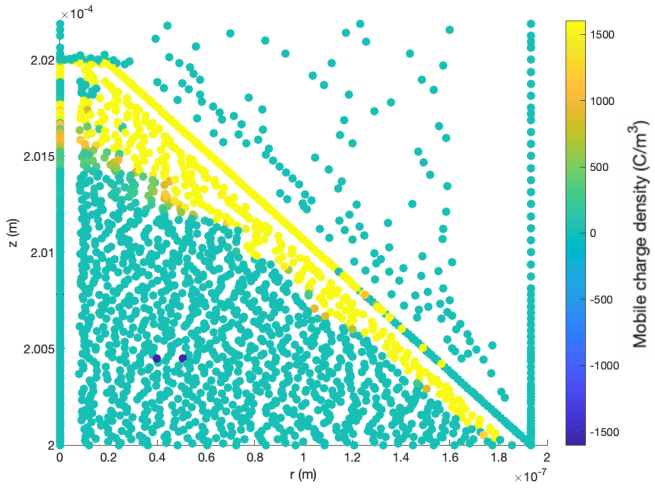

Figure 4.2: Scatter Diagram of mobile charges at 2000V contact voltage ($r = 20nm$; Doping Concentration $N_D = 1\text{e}16cm^{-3}$).

4.1.1 Varying the Radius of GaN Tip

Cases are simulated where the radius of the tip has been increased to $200nm$, with every other parameter remaining the same. Figure 4.3 shows a scatter diagram of mobile charges of APT environment with $200nm$ radius GaN tip at 2000V contact voltage. Under the same

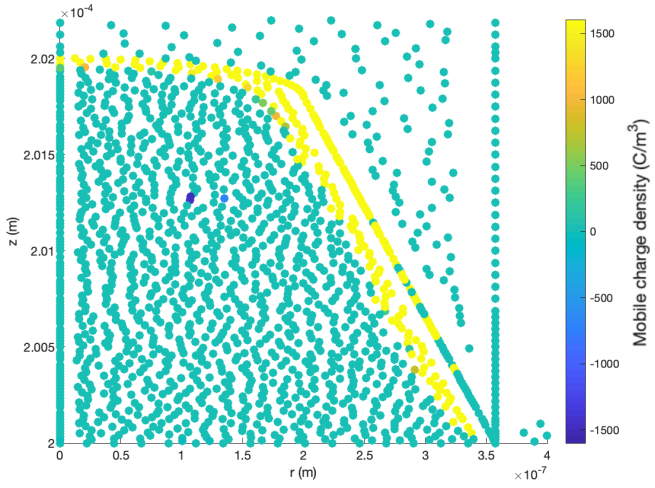

Figure 4.3: Scatter Diagram of mobile charges at 2000V contact voltage (Tip radii $r = 200nm$; Doping Concentration $N_D = 1\text{e}16cm^{-3}$).

color bar scale, it is clear that a positive charge layer, although thinner than the one shown

in figure 4.2, has shown at the edge, with the rest of the tip being depleted. Taking a further look into the k factor of $200nm$ cases, table 4.2 shows the k factor and minimum electric field to the corresponding voltages. With the increased radius, k factor drops by about 0.8 but still lies within the metallic range $1.5 < k < 8.5$.

Table 4.2: Table of voltages, electric field, and k-factor of 200-nm radii GaN tip at n-type doping concentration of $1\text{e}16cm^{-3}$.

Contact Voltages[kV]	Minimum Electric Field[$\times 10^{09}$ V/m]	k-factor
2	-2.972	3.3653
4	-5.965	3.3531
6	-8.958	3.3491
8	-11.95	3.3471
10	-14.94	3.3460

4.1.2 Varying the Doping Concentration within the Tip

Varying the doping concentration within the semiconductor tip also helps to show the charges inversion phenomenon as well as further explain the situation. The following cases use the same physical parameters as the simulations in section 4.1, with the n-type doping increased increased from $1\text{e}16cm^{-3}$ to $1\text{e}18cm^{-3}$. At the same 2000V contact voltage, figure 4.4 shows the mobile charge scatter diagram. The mobile charge distribution in this case shows even more information as a third layer of charges (labeled purple) is observed. This layer of charges are negative, which is a layer of mobile charges expected to be observed for a n-type doping semiconductor material. To compare with the k factor, table 4.3 shows the k factor of the model under increased doping concentration. The k factor in the higher doping concentration cases not only are in the designated range but also are close to the ones in the original model. Particularly at 6000V, 8000V, and 10000V, k factor become the same.

In order to understand why GaN tip exhibits such similar behavior as a metallic tip, first we need to understand why a layer of positive mobile charges has been observed in

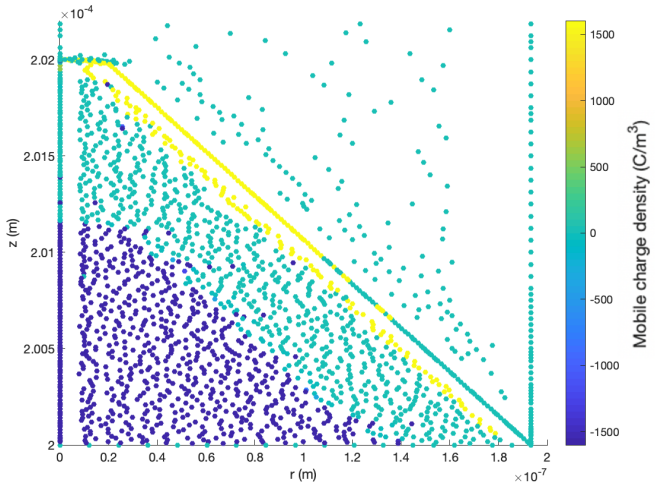

Figure 4.4: Scatter Diagram of mobile charges at 2000V contact voltage (Tip radii $r = 20nm$, Doping Concentration $N_D = 1\text{e}18cm^{-3}$).

Table 4.3: Table of voltages, electric field, and k-factor of 20-nm radii GaN tip at n-type doping concentration of $1\text{e}18cm^{-3}$.

Contact Voltages[kV]	Apex Electric Field[$\times 10^{10}$ V/m]	k-factor
2	2.475	4.0403
4	4.858	4.1169
6	7.271	4.1257
8	9.699	4.1240
10	12.13	4.1230

an area where negative charges are supposed to be observed. Under high bias, the mobile electron concentration is depleted and eventually inverted into a hole layer, called the inversion layer. This is analogous to a Metal-Oxide-Semiconductor capacitor, where inversion layer forms under biasing. We believe that the high conductivity inversion layer acts like a metallic tip, thus explaining why the k factor for the semiconductor tip falls within the range for metallic tips. To elucidate that explanation, we investigate the behavior of this model in low contact voltages, to explore the voltage at which the depletion and inversion layers form.

4.2 GaN Tip under Low Contact Voltages

In order to prove that the formation of inversion layer improves conductivity of the GaN semiconductor tip so it behaves much like metallic tips under high voltage atom probe tomography, we have to find out at what level of contact voltage does the inversion layer start to form. This section outlines the results for scatter plots of mobile charges within the tip at contact voltage difference from 0V to 50V, as well as shows proof on the occurrence of inversion layer, and shows the charge density change at the symmetrical axis of the tip apex.

4.2.1 Contact Voltage from 0V to 10V

The first low contact voltage simulation is done at 0V, with the sim to verify the behavior of mobile charges under no bias condition. Under no contact voltages, a net charge of 0 should be seen anywhere within the GaN tip, using equation 3.6. Combining with equation 3.17 and equation 3.47, the mobile net charge density within the GaN tip at zero contact voltage should be $\rho_{GaN,mobile} = -e \cdot N_D$. At a n-type doping concentration of $1\text{e}16cm^{-3}$, the value is $\rho_{GaN,mobile} = -1600C/m^3$. The top-left diagram of figure 4.5 verifies the mobile charge behavior at 0 volt. The contact voltage difference is then gradually increased at 1V step. It can be seen in diagram (2) of figure 4.5 that beginning at voltage as low as 1V, negative charges at the right edge of the tip begin to move away (where the colors of the nodes begin shifting from purple to light blue). At 5V standing voltage, a layer of depleted charge (labeled green at diagram (3) of figure 4.5) has formed at the right edge while the majority of the tip area is still filled with negative charges. As the voltage increases further, the depletion region becomes thicker, as can be foreseen. Diagram (4) of figure 4.5 shows the mobile charge behavior at 10-volt contact difference, with which the layer of the depletion has taken a majority of area of the tip.

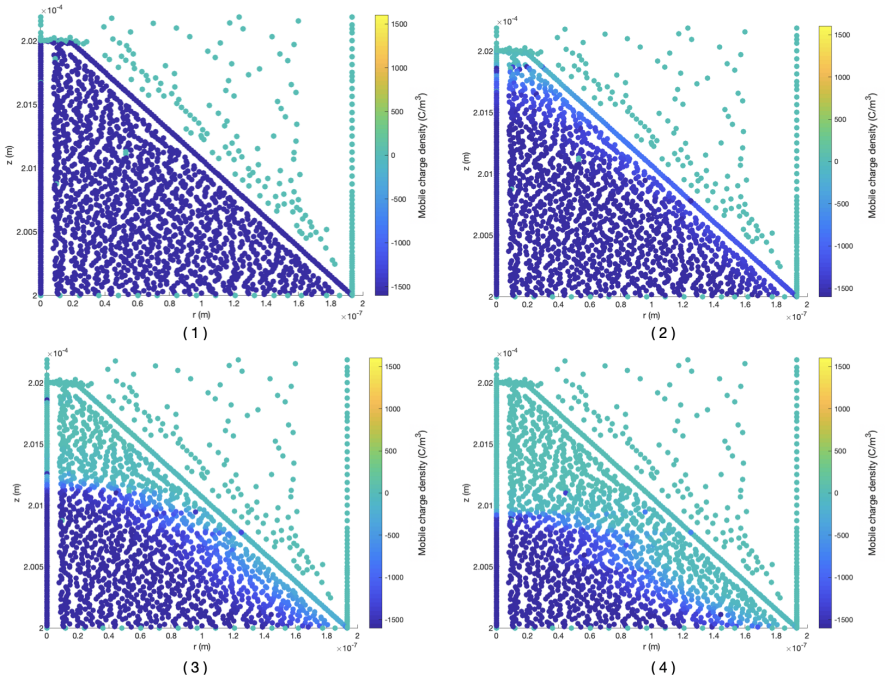

Figure 4.5: Scatter Diagrams of mobile charges at (1) 0V, (2) 1V, (3) 5V, (4) 10V contact voltages (Tip radii $r = 20nm$; Doping Concentration $N_D = 1\text{e}16cm^{-3}$).

4.2.2 Contact Voltage from 20V to 50V

With the gradual increase of contact voltages for simulation, it is predictable that the depletion layer will reach a maximum thickness, and an inversion layer of holes will form at the surface for sufficiently high applied voltages. Figure 4.6 shows scatter diagrams of mobile charge at 4 difference voltage levels: 20 volts, 23 volts, 30 volts, and 50 volts. At 20V contact difference, there is a small amount of positive charges observed at the tip apex, which notes the first occurrence of inversion charge. Taken further, a larger area of positive charges pops up at 23 volts, occurring in the area of the tip nearest to the local electrode. Strictly speaking, the layer of such positive charges should be regarded as the occurrence of inversion layer. Keeping the increase of standing voltages, at 30 V, a quite visible layer of positive charges can be seen, while the layer of negative charges keeps shrinking to a thin strip. The layer of negative charges can be barely observed or almost disappeared at 50V contact difference. The significance of these can be revealed on calculating the k-factor

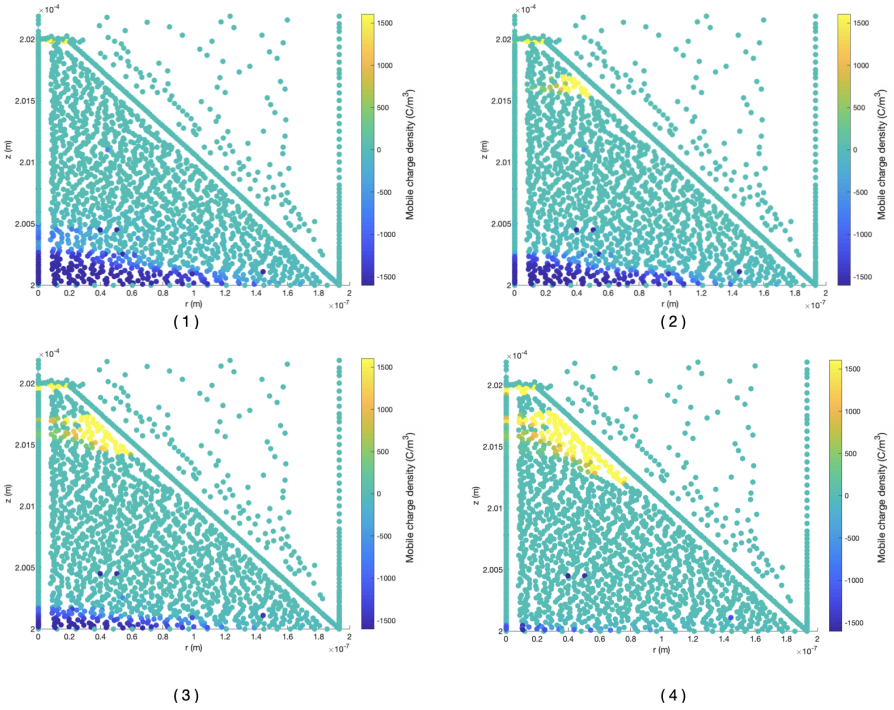

Figure 4.6: Scatter Diagrams of mobile charges at (1) 20V, (2) 23V, (3) 30V, (4) 50V contact voltages (Tip radii $r = 20nm$; Doping Concentration $N_D = 1\text{e}16cm^{-3}$).

with the respected electric field at apex. Table 4.4 shows the k factor at several important steps of contact voltage. Related to the observance of inversion layer, k factor is seen to

Table 4.4: Table of contact voltage and corresponding k-factor of 20-nm radii GaN tip at n-type doping concentration of $1\text{e}16cm^{-3}$.

Contact Voltage[V]	k-factor
1	2.0515
5	5.8821
10	8.8741
20	9.0736
23	7.8765
30	6.6798
50	5.6033

increase with low voltage up to 20 volts, where k factor peaks at the first observance of positive charges. After that, k factor drastically reduces along with the increasing contact voltage. Starting at 50V, the rate of reduction of k factor starts to slow to 0.2 per 10V step.

Figure 4.7 shows how the k factor depends on the applied voltage. Beginning with the first appearance of the inversion layer at about 20 V, the k factor gradually converges towards a constant value as the inversion layer gradually dominates the electrostatic response of the tip.

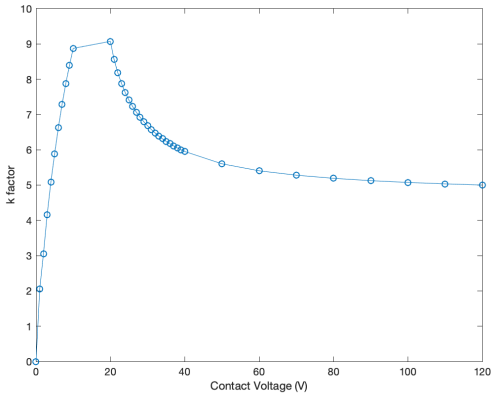

Figure 4.7: K factor distribution with Contact Voltage changing from 0V to 120V.

An alternative way to visualize the growth of the depletion region and the formation of the inversion layer as a function of the applied voltage can be seen in the figures below. Figure 4.8 shows plots of the mobile charge density along the axis of symmetry of the cylindrical tip (the z-axis) from the base to the apex of the tip at a contact voltage difference of 0V, 10V, 23V, and 30V. Although some numerical artifacts can be observed in the data, the graphs do show the formation of the depletion and inversion layers. Diagram (2) of figure 4.8 shows the depletion layer starts to form at almost half of the tip length at contact voltage difference of 10 volts. At 23 volt contact difference, where the inversion layer is observed at the first instance, a sharp spike of charge density at the tip apex can be observed on the diagram (3) of figure 4.8. At this point, the layer of negative charges can still be seen at the bottom of the tip, however, the size of its occupation has been reduced. On the fourth diagram on figure 4.8, where contact voltage difference has been increased to 50 volts, the spike of the inversion layer has grown drastically while the length of occupation by the negative charge layer has shrunk so small that it can barely be observed. This matches the

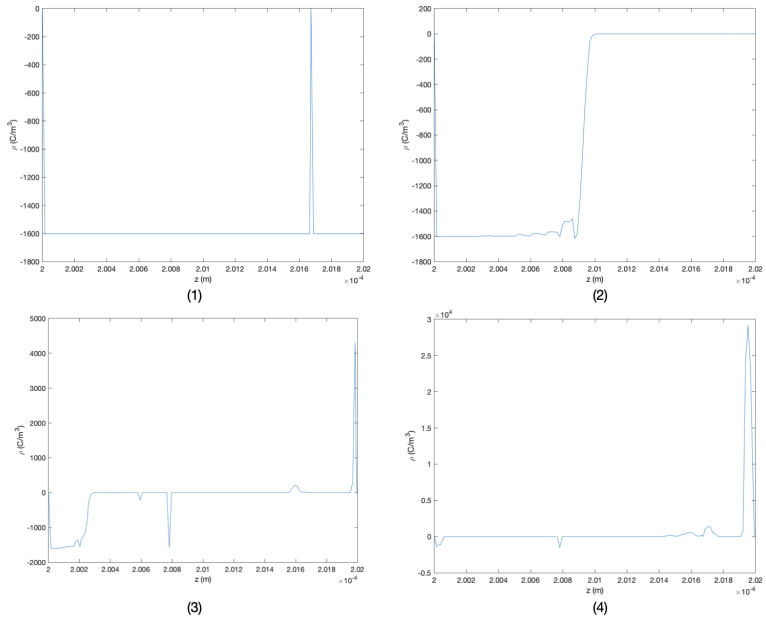

Figure 4.8: On-axis mobile charge density at (1) 0V, (2) 10V, (3) 23V, (4) 50V contact voltage difference (Tip radii $r = 20nm$; Doping Concentration $N_D = 1\text{e}16cm^{-3}$).

previous result where the negative charge accumulation layer disappears at 50 volt contact difference.

4.3 Dielectrics under high voltages

To further explore the theory that the formation of the inversion layer within the GaN samples at high applied voltages accounts for the metal-like values of the k-factor, simulations were run with insulating materials that are unable to generate inversion layers. This section performs results on simulations with dielectric materials as the tip. The first one simulated is silicon dioxide, SiO_2. The second one is a nonphysical material with all of the properties of our GaN samples, except zero doping and zero mobile charge density at all biases. We call this material 'insulator-GaN, which bears all the parameters with the normal semiconductor GaN except its semiconductor factor is disabled, is created to perform simulation.

4.3.1 Results of SiO2 in high voltages

Silicon dioxide is an insulator of high band gap energy $8.76eV$ and used widely as an Insulator layer in electronic devices. Its low conductivity makes it a suitable material as an dielectric tip in APT environment. To ensure an controlled simulation, both the tip dimensions and the APT contact dimensions are unchanged. Figure 4.9 shows the mobile charge density scatter of SiO2 tip in 2000 volts contact difference. It can be shown that, under

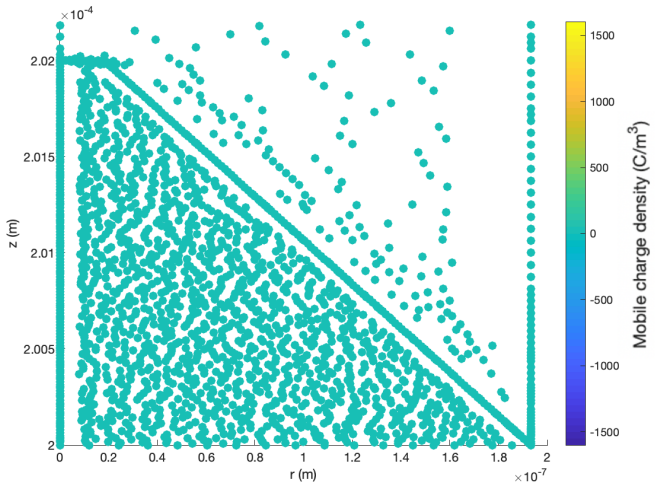

Figure 4.9: Mobile charge density scatter diagram of SiO2 at 2000V contact difference.

such high external biasing, there is still no mobile charge seen within the tip. Furthermore, SiO2 k-factor is far outside the range expected for metallic tips. Table 4.5 shows a comparison of k factor under high voltages between semiconductor GaN tip and SiO2 tip. The k

Table 4.5: Table showing comparisons of k factor of semiconductor GaN and SiO2 under high voltages (Both have the same tip layout and are under the same APT setup).

Contact Voltages[kV]	k-factor of semiconductor GaN	k-factor of SiO2
2	4.1425	89.4914
4	4.1297	89.4914
6	4.1258	89.4914
8	4.1240	89.4914
10	4.1230	89.4914

factor for SiO2 tip is much higher than k factor for semiconductor GaN as well as all SiO2 k factor are out of the designated range. This is an expected result as insulator is supposed to behave differently than metals. In addition, the lack of inversion layer seen on SiO2 tip under high voltage also denotes a higher k factor as the electric field at the tip apex is seen some degree short from that of semiconductor GaN tip.

4.3.2 Results of 'Insulator-GaN' in high voltages

It is possible that the difference in material parameters such as the permittivity, rather than the difference in conductivity, might account for the different behavior of SiO2 and GaN. Therefore, in order to eliminate this possibility, a nonphysical material Insulator-GaN is created. Insulator-GaN has exactly the same material parameters as semiconductor GaN, but it is undoped and has no mobile charge (it is insulating). Figure 4.10 shows the mobile charge scatter diagram of insulator-GaN at 2000 volt contact voltage. Just like the case in

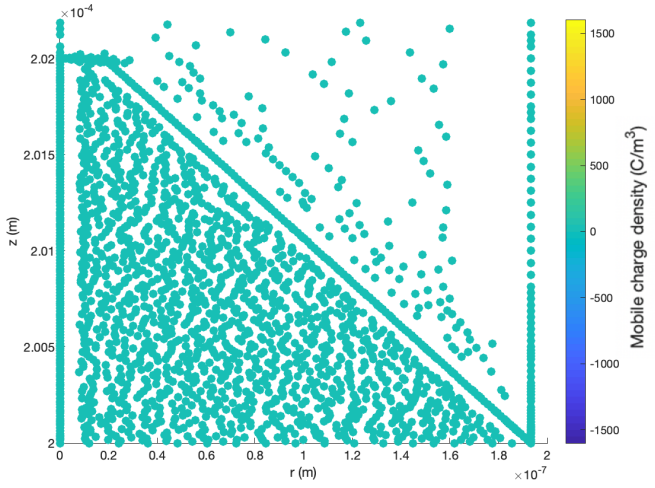

Figure 4.10: Mobile charge density scatter diagram of insulator-GaN at 2000V contact difference.

SiO2, no mobile charge is seen in insulator-GaN case under high contact voltage. The lack of mobile charge significantly reduces the electric field generated and increase its k factor. Table 4.6 below shows the k factor comparison between two types of GaN tip. It is seen from the data that k factor for Insulator-GaN is is constant with increasing voltage and is

Table 4.6: Table showing comparisons of k factor of Semiconductor-GaN and Insulator-GaN under high voltages (Both have the same tip layout and are under the same APT setup).

Contact Voltages[kV]	k-factor of Semiconductor-GaN	k-factor of Insulator-GaN
2	4.1425	177.1795
4	4.1297	177.1795
6	4.1258	177.1795
8	4.1240	177.1795
10	4.1230	177.1795

considerably higher than for semiconductor-GaN. the apex electric field in Insulator-GaN is considerably smaller than for semiconductor-GaN, since the lack of an inversion layer prevents the metal-like concentration of the electric field at the sample tip. As a result, the on-axis electric field for such material behaves differently from its semiconductor form. Figure 4.11 shows the on-axis electric field at 2 kV contact difference.

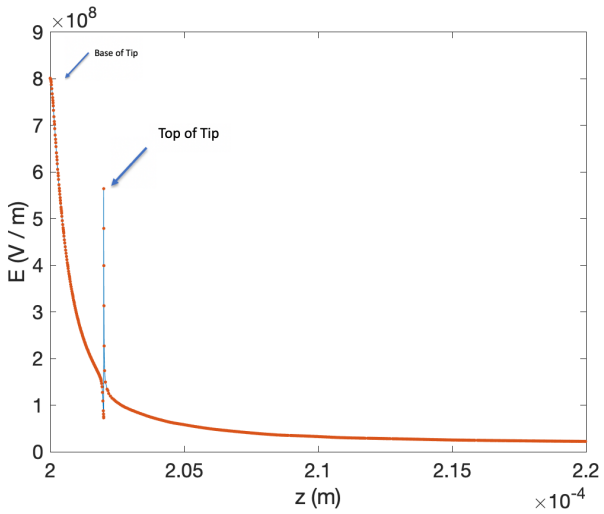

Figure 4.11: Axial Electric field at 2000V SV with Insulator-GaN tip. (Tip radii $r = 20nm$).

Compared to the on-axis electric field shown in figure 4.1, several important differences can be noted when comparing the two figures. At the base of the tip, the electric field on semiconductor-GaN tip is close to zero, while electric field on insulator-GaN is at its highest in magnitude. At the tip apex, electric field on semiconductor-GaN tip reaches peak in

magnitude, which results in a low k factor in the designated range, while the electric field on insulator-GaN is observed to be greatly reduced at at the tip apex. The difference in where electric field reaches peak in magnitude is responsible for why k factor behaves differently in these two materials. Additionally, the tip apex electric field magnitude on insulator-GaN is about 40 times smaller than the tip apex electric field magnitude on semiconductor-GaN.

Direct comparison of the results for the semiconductor-GaN and insulator-GaN tips helps establish the theory that the formation of an inversion layer is responsible for the metal-like k-factor of semiconductor-GaN samples.

CHAPTER 5
CONCLUSION

In this thesis, the charge distribution and electric field within a n-type doping gallium nitride tip in an atom probe tomographic environment have been studied using an self-consistent mathematical simulation of Poisson's equations. This nonlinear method provides electrostatic potential for every node bound by the rigorous modeling of the APT, from which it generates mobile charge density and electric field results. Using a simple approximation model that calculate the apex electric field given a certain applied voltage, we are able to study the electrostatics surrounding the apex of the semiconductor tip, which the character of field evaporation process in APT is strongly dependent on. By comparing the k-factor, a dimensionless fitting parameter, between semiconductor tip and previous-studied metallic materials, we have found that sharp n-doped GaN tip shows close characteristics as metallic tips, regardless of the variations in tip radius or tip doping concentration. By analyzing the mobile charge density of the environment surrounding the tip, a positive charge inversion layer is observed at the outer edge of the semiconductor tip and apex surface at sufficiently high applied voltages. The formation of inversion layer is accounted for why sharp rounded-tip semiconductor behaves similarly as sharp metallic tips do under atom probe tomography. Additionally, to help eliminate other possible explanations, a non-physical dielectric material that is unable to generate inversion layer is created for comparisons of on-axis electric field, mobile charge density distribution and k factor.

CHAPTER 6
FUTURE WORK

Although using 3D cylindrical-symmetric model can present a rigorous simulation and generate close-to experimental data for semiconductor tip in an atom probe tomography, one characteristics specifically found in III-Nitride semiconductor might affect the data accuracy under special circumstances.

Spontaneous polarization is a characteristic usually found in III-nitride semiconductors due to the intrinsic asymmetry of bonding in their wurtzite crystal structure[39]. Under spontaneous polarization effect, positive and negative charges generated at the interfaces of III-nitride materials would be uneven, which creates net electrical dipoles under no bias. This project did not include the effect of spontaneous polarization occurring in gallium nitride as it is impossible to generate uneven charge within 3D cylindrical-symmetric model. However, the spontaneous polarization parameter for gallium nitride is $P_{SP,GaN} = -0.034 C/m^2$ [40], a value so small that can be neglected in tomographic environment which operates under high contact voltages. Therefore, the data and results generated in this project withstands.

On the other hand, spontaneous polarization parameters are higher in other III-nitride semiconductor such as aluminum nitride (AlN) and indium nitride (InN) along with their related alloys[41]. Such difference will form inaccuracy to certain data and is worth looking into. In these cases, using a 2D planar model presented in figure 3.3 for simulation might benefit its accuracy. Currently, the team is undergoing such simulations to study the effect by spontaneous polarization in other III-nitride alloys.

REFERENCES

[1] E. W. Müller, J. A. Panitz, and S. B. McLane, "The atom probe field ion microscope," *Review of Scientific Instruments*, vol. 39, no. 1, pp. 83–86, 1968.

[2] R. J. H. Morris, R. Cuduvally, D. Melkonyan, C. Fleischmann, M. Zhao, L. Arnoldi, P. van der Heide, and W. Vandervorst, "Toward accurate composition analysis of GaN and alGaN using atom probe tomography," *Journal of Vacuum Science & Technology B*, vol. 36, no. 3, 03F130, 2018.

[3] J. R. Shewchuk, "Triangle: Engineering a 2D Quality Mesh Generator and Delaunay Triangulator," in *Applied Computational Geometry: Towards Geometric Engineering*, ser. Lecture Notes in Computer Science, vol. 1148, Springer-Verlag, May 1996, pp. 203–222.

[4] ——, "Delaunay refinement algorithms for triangular mesh generation," *Computational Geometry*, vol. 22, no. 1, pp. 21 –74, 2002, 16th ACM Symposium on Computational Geometry.

[5] T. F. Kelly and M. K. Miller, "Atom probe tomography," *Review of Scientific Instruments*, vol. 78, no. 3, p. 031 101, 2007.

[6] T. F. Kelly and J. A. Panitz, "The first fifty years of atom probe," *Microscopy Today*, vol. 25, no. 3, 1217, 2017.

[7] G. L. Kellogg and T. T. Tsong, "Pulsed-laser atom-probe field-ion microscopy," *Journal of Applied Physics*, vol. 51, no. 2, pp. 1184–1193, 1980.

[8] J. A. P. Thomas F. Kelly, *A brief history of atom probe*, 2016.

[9] J. Panitz, "Imaging atom-probe mass spectroscopy," *Progress in Surface Science*, vol. 8, no. 6, pp. 219 –262, 1978.

[10] J. A. Panitz, "The 10 cm atom probe," *Review of Scientific Instruments*, vol. 44, no. 8, pp. 1034–1038, 1973.

[11] J. A. Panitz and J. A. Foesch, "Areal detection efficiency of channel electron multiplier arrays," *Review of Scientific Instruments*, vol. 47, no. 1, pp. 44–49, 1976.

[12] A. Cerezo and et al., "Materials analysis with a position-sensitive atom probe," *Journal of Microscopy*, vol. 154, no. 3, pp. 215–225, 1989.

[13] M. Miller, "Implementation of the optical atom probe," *Surface Science*, vol. 266, no. 1, pp. 494 –500, 1992.

[14] D. Blavette, B. Deconihout, A. Bostel, J. M. Sarrau, M. Bouet, and A. Menand, "The tomographic atom probe: A quantitative three-dimensional nanoanalytical instrument on an atomic scale," *Review of Scientific Instruments*, vol. 64, no. 10, pp. 2911–2919, 1993.

[15] D. Blavette, A. Bostel, J. M. Sarrau, B. Deconihout, and A. Menand, "An atom probe for three-dimensional tomography," *Nature*, vol. 363, no. 6428, pp. 432–435, 1993.

[16] O. Nishikawa and M. Kimoto, "Toward a scanning atom probe – computer simulation of electric field –," *Applied Surface Science*, vol. 76-77, pp. 424 –430, 1994.

[17] O. Nishikawa, M. Kimoto, M. Iwatsuki, and Y. Ishikawa, "Development of a scanning atom probe," *Journal of Vacuum Science & Technology B: Microelectronics and Nanometer Structures Processing, Measurement, and Phenomena*, vol. 13, no. 2, pp. 599–602, 1995.

[18] T. F. Kelly, P. P. Camus, D. J. Larson, L. M. Holzman, and S. S. Bajikar, "On the many advantages of local-electrode atom probes," *Ultramicroscopy*, vol. 62, no. 1, pp. 29 –42, 1996.

[19] "Local electrode atom probes," *Materials Characterization*, vol. 44, no. 1, pp. 59 –85, 2000.

[20] A. Giddings, T. Prosa, D. Olson, P. Clifton, and D. Larson, "Reverse engineering at the atomic scale: Competitive analysis of a gallium-nitride-based commercial light-emitting diode," *Microscopy Today*, vol. 22, no. 5, 1219, 2014.

[21] A. Cerezo, C. R. M. Grovenor, and G. D. W. Smith, "Pulsed laser atom probe analysis of semiconductor materials," *Journal of Microscopy*, vol. 141, no. 2, pp. 155–170,

[22] B. Gault, F. Vurpillot, A. Vella, M. Gilbert, A. Menand, D. Blavette, and B. Deconihout, "Design of a femtosecond laser assisted tomographic atom probe," *Review of Scientific Instruments*, vol. 77, no. 4, p. 043 705, 2006.

[23] J. H. Bunton, J. D. Olson, D. R. Lenz, and T. F. Kelly, "Advances in pulsed-laser atom probe: Instrument and specimen design for optimum performance," *Microscopy and Microanalysis*, vol. 13, no. 6, 418427, 2007.

[24] B. Gault, "A brief overview of atom probe tomography research," *Applied Microscopy*, vol. 46, no. 3, pp. 117–126, 2016.

[25] "Book listing of crc handbook of chemistry and physics, 92nd ed., 20112012," *Journal of the American Chemical Society*, vol. 133, no. 34, pp. 13 766–13 766, 2011.

[26] K. Ahi, "Review of GaN-based devices for terahertz operation," *Optical Engineering*, vol. 56, p. 1, Sep. 2017.

[27] K. Ueno, A. Kobayashi, and H. Fujioka, "Characteristics of unintentionally doped and lightly Si-doped GaN prepared via pulsed sputtering," *AIP Advances*, vol. 9, no. 7, p. 075 123, 2019.

[28] L. B. Rowland, K. Doverspike, and D. K. Gaskill, "Silicon doping of GaN using disilane," *Applied Physics Letters*, vol. 66, no. 12, pp. 1495–1497, 1995.

[29] H. M. Ng, D. Doppalapudi, T. D. Moustakas, N. G. Weimann, and L. F. Eastman, "The role of dislocation scattering in n-type GaN films," *Applied Physics Letters*, vol. 73, no. 6, pp. 821–823, 1998.

[30] E. F. Schubert, I. D. Goepfert, W. Grieshaber, and J. M. Redwing, "Optical properties of Si-d oped GaN," *Applied Physics Letters*, vol. 71, no. 7, pp. 921–923, 1997.

[31] T. Zhu and R. A. Oliver, "Unintentional doping in GaN," *Phys. Chem. Chem. Phys.*, vol. 14, pp. 9558–9573, 27 2012.

[32] S. Nakamura, "GaN growth using GaN buffer layer," *Japanese Journal of Applied Physics*, vol. 30, no. Part 2, No. 10A, pp. L1705–L1707, Oct. 1991.

[33] N. Sanford, P Blanchard, M. Brubaker, K. Bertness, A. Roshko, J. Schlager, R. Kirchhofer, D Diercks, and B. Gorman, "Laser-assisted atom probe tomography of mbe grown GaN nanowire heterostructures," *Physica status solidi (c)*, vol. 11, Feb. 2014.

[34] B. N. Delaunay, "Sur la sphère vide.," *BULL. ACAD. SCI. URSS*, vol. 1934, no. 6, pp. 793–800, 1934.

[35] D. J. Larson, T. J. Prosa, R. M. Ulfig, B. P. Geiser, and T. F. Kelly, "Design and instrumentation," in *Local Electrode Atom Probe Tomography: A User's Guide*. New York, NY: Springer New York, 2013, pp. 55–77, ISBN: 978-1-4614-8721-0.

[36] S. T. Loi, B. Gault, S. P. Ringer, D. J. Larson, and B. P. Geiser, "Electrostatic simulations of a local electrode atom probe: The dependence of tomographic reconstruction parameters on specimen and microscope geometry," *Ultramicroscopy*, vol. 132, 107113, Sep. 2013.

[37] P. J. Birdseye and D. Smith, "The electric field and the stress on a field-ion specimen," *Surface Science*, vol. 23, no. 1, pp. 198 –210, 1970.

[38] T. F. Kelly, “Atom-probe tomography,” in *Springer Handbook of Microscopy*, P. W. Hawkes and J. C. H. Spence, Eds. Cham: Springer International Publishing, 2019.

[39] F. Bernardini, V. Fiorentini, and D. Vanderbilt, “Spontaneous polarization and piezoelectric constants of III-V nitrides,” *Phys. Rev. B*, vol. 56, R10024–R10027, 16 Oct. 1997.

[40] ——, “Accurate calculation of polarization-related quantities in semiconductors,” *Phys. Rev. B*, vol. 63, pp. 193–201, 19 Apr. 2001.

[41] S.-H. Park and S.-L. Chuang, “Spontaneous polarization effects in wurtzite GaN/AlGaN quantum wells and comparison with experiment,” *Applied Physics Letters*, vol. 76, no. 15, pp. 1981–1983, 2000.